Single-particle tracking and machine-learning classification reveals heterogeneous Piezo1 diffusion

Vivek Tyagi[1, 7], Alan T. Ly[2, 6, 7], Gabriella A. Bertaccini[2, 6], Elizabeth L. Evans[2, 6], J. Alfredo Freites[3], Douglas J. Tobias[3, *], and Medha M. Pathak[2, 4, 5, 6, *]

[1]Department of Materials Science & Engineering, UC Irvine, Irvine, California
[2]Department of Physiology & Biophysics, UC Irvine, Irvine, California
[3]Department of Chemistry, UC Irvine, Irvine, California
[4]Department of Biomedical Engineering, UC Irvine, Irvine, California
[5]Center for Complex Biological Systems, UC Irvine, Irvine, California
[6]Sue and Bill Gross Stem Cell Research Center, UC Irvine, Irvine, California
[7]These authors contributed equally to this work.
[*]Correspondence: medhap@uci.edu and douglas.tobias@uci.edu

ABSTRACT

The mechanically-activated ion channel Piezo1 is involved in numerous physiological processes. Piezo1 is activated by diverse mechanical cues and is gated by membrane tension. The channel has been found to be mobile in the plasma membrane. We employed single particle tracking (SPT) of endogenously-expressed, tdTomato-tagged Piezo1 using Total Internal Reflection Fluorescence Microscopy in two cell types, mouse embryonic fibroblasts and liver sinusoidal endothelial cells. Application of SPT unveiled a surprising heterogeneity of Piezo1 mobility in the plasma membrane. Leveraging a machine learning technique, Piezo1 trajectories were sorted into distinct classes (“mobile,” “intermediate,” and “trapped”) by partitioning features that describe the geometric properties of a trajectory. To evaluate the effects of the plasma membrane properties on Piezo1 diffusion, we manipulated membrane composition by depleting or supplementing cholesterol or by adding margaric acid to stiffen the membrane. To address effects of channel activation on Piezo1 mobility, we treated cells with Yoda1, a Piezo1 agonist, and GsMTx-4, a channel inhibitor. We collected thousands of trajectories for each condition, and found that “mobile” Piezo1 in cells supplemented with cholesterol or margaric acid exhibited decreased mobility, whereas Piezo1 in cholesterol-depleted membranes demonstrated increased mobility, compared to their respective controls. Additionally, activation by Yoda1 increased Piezo1 mobility and inhibition by GsMTx-4 decreased Piezo1 mobility compared to their respective controls. The “mobile” trajectories were analyzed further by fitting the time-averaged mean-squared displacement as a function of lag time to a power-law model, revealing Piezo1 consistently exhibits anomalous subdiffusion. This suggests Piezo1 is not freely mobile, but that its mobility may be hindered by subcellular interactions. These studies illuminate the fundamental properties governing Piezo1 diffusion in the plasma membrane and set the stage to determine how specific cellular interactions may influence channel activity and mobility.

SIGNIFICANCE Piezo1 is a mechanically-activated ion channel that regulates a number of physiological processes. Here we examine a fundamental biophysical property of Piezo1 - its movement in the plasma membrane. We find that the mobility of Piezo1 is surprisingly heterogeneous, with some Piezo1 puncta showing high mobility, some very limited mobility, and a third class showing intermediate mobility. Cholesterol depletion from the plasma membrane increases Piezo1 mobility while cholesterol or margaric acid supplementation decreases mobility. Yoda1 treatment increases Piezo1 mobility whereas GsMTx-4 treatment decreases channel mobility.

INTRODUCTION

The Piezo family of ion channels was discovered over a decade ago and was found to sense and transduce mechanical forces (1). The importance of Piezo proteins is underscored by the fact that they are highly conserved in many species, including mammals, plants, and protozoa, and are expressed in a wide range of tissues. Piezo channels activate in response to mechanical cues and cause cationic influx (1) and regulate a number of crucial biological processes. These proteins are critical in vascular development (2, 3), lymphatic valve development (4), bone formation (5), blood pressure baroreflex (6), mechanical itch (7) and touch (8, 9), proprioception (10), tactile and mechanical pain (11, 12), skin wound healing (13), and neural stem cell differentiation (14). Knockouts of Piezo1 are embryonic lethal (2, 3), and Piezo1 mutations are associated with several diseases, including dehydrated hereditary stomatocytosis, and lymphatic dysplasia (15, 16).

The homotrimeric Piezo1, with its triple-blade, propeller-like architecture, has a unique structure compared to other known membrane proteins (17–20). The propeller blades consist of repeating four-transmembrane-helix-containing bundles, and are linked to the central pore by the beam and anchor domains (17). Structural and computational studies of Piezo1 reveal that the channel structure causes local distortion of the membrane, thereby inducing membrane curvature and causing the membrane to adopt a striking bowl-like characteristic (19, 21). Membrane tension has been shown to gate the channel (22–24), demonstrating that the channel directly senses forces on the lipid bilayer.

We previously reported that internal cell-generated traction forces from the actomyosin cytoskeleton can activate Piezo1 in the absence of external mechanical stimuli (14, 25). Using a Piezo1-tdTomato reporter mouse model where the tdTomato fluorophore is knocked in at the Piezo1 C-terminus, we found that the Piezo1 protein is not restricted to focal adhesions, the location of traction forces, and that the channel is surprisingly mobile (25). Ridone *et al.* similarly found that the channel was mobile using heterologously-expressed Piezo1-GFP, and further showed that cholesterol depletion via methyl-β-cyclodextrin (MBCD) increased channel diffusion and disrupted clustering of Piezo1 (26).

The plasma membrane through which Piezo1 diffuses is a complex environment with considerable structural heterogeneity which may give rise to a variety of interactions between Piezo1 and its surrounding environment (27, 28). Understanding the nature of Piezo1 mobility can help to elucidate these Piezo1-membrane interactions and thereby the underlying force sensing mechanisms.

Here, we report single-particle tracking (SPT) of endogenously expressed Piezo1-tdTomato channels. Visual examination reveals heterogeneous trajectories that could be classified into three broad categories based on their spatial extent: “mobile” class wherein trajectories displayed relatively large spatial extent, “trapped” trajectories limited to a small area, and an “intermediate” class with a spatial extent in-between the other two categories. We implemented a supervised machine learning approach to objectively classify thousands of trajectories based on their geometric properties. We show that pharmacological perturbations to the lipid membrane composition and to channel activity result in measurable changes to Piezo1 mobility in the “mobile” class of trajectories. The “mobile” class was also found to be subdiffusive across all the tested experimental conditions. Our results demonstrate that membrane composition and channel activity may play a key role in regulating Piezo1 mobility.

MATERIALS AND METHODS

Mouse Embryonic Fibroblast (MEF) Harvesting and Culture

MEF cells were isolated from a reporter mouse (JAX stock 029214) with a tdTomato knock-in at the C-terminus of the endogenous Piezo1 channel (2). Mice were considered embryonic day 0.5 upon vaginal plugging. Fibroblast cells were harvested from embryos by separating the head, limbs, and tail from the embryo at embryonic day 12.5 in 33 mM D-(+)-glucose (Sigma-Aldrich, G-6152) and 1% Penicillin-Streptomycin (10,000 U/mL; Gibco, 15140122) in Dulbecco’s Phosphate-Buffered Saline (Gibco, 14-190-250). The remaining tissue was spun at 260g for 5 min, and the supernatant was aspirated. These cells were cultured in DMEM (ThermoFisher Scientific, 11960-051) with 15% fetal bovine serum (Omega Scientific, FB-12), 1x GlutaMax (ThermoFisher Scientific, 35050-061), 1 mM sodium pyruvate (ThermoFisher Scientific, 11360-070), and 1x non-essential amino acid solution (ThermoFisher Scientific, 11140-050) in a sterile environment at 37°C with 5% CO_2. Cells were plated in a T-25 cell culture flask (Eppendorf, 0030710126) coated with 0.1% gelatin solution (Fisher Scientific, ES-006-B). Media was changed 1 hour after plating. MEF cells containing Piezo1-tdTomato were passaged using TrypLE Express (ThermoFisher, 12604013) to dissociate the cells and were spun at 260g for 5 min. Cells were then counted using a hemocytometer and 7,500-10,000 cells between the passages of 3-7 were plated on the 14mm glass region of #1.5 glass-bottom dishes (Mat-Tek Corporation) coated with 10 µg/mL fibronectin (Fisher Scientific, CB-40008A). Media was changed following 2h and every 48h until imaging experiments. Cells were maintained in a 5% CO_2 incubator at 37ºC for at least 72h prior to imaging.

Mouse Liver Sinusoidal Endothelial (mLSEC) Isolation and Culture

mLSECs were isolated using an immunomagnetic separation technique. A mouse liver was thoroughly minced using scalpel blades and resuspended in a dissociation solution containing 9 mL 0.1% collagenase II, 1 mL 2.5 U ml-1 dispase, 1 µM $CaCl_2$ and 1 µM $MgCl_2$ in Hanks Buffer solution. The tissue-dissociation mix was incubated at 37ºC for 50 mins in a tube rotator to provide continuous agitation. Following this enzymatic digestion, the mix was passed through 70 and 40 µm cell strainers to remove undigested tissue. Cells were washed twice in PEB buffer containing phosphate-buffered saline solution (PBS), EDTA 2mM and 0.5% BSA, pH 7.2. The washed pellets were resuspended in 1 mL PEB buffer and 30 µL CD146 microbeads (Miltenyi Biotech) at 4ºC for 15 min under continuous agitation. CD146 is a membrane protein marker for endothelial cells and is highly expressed in mLSECs. Following incubation, the solution was passed through an LS column (Miltenyi Biotech) primed with PEB buffer. The column was washed 3 times with 5 mL PEB buffer and the CD146 negative eluate was removed. CD146 positive cells were retained in the column and flushed with 5 mL warmed EGM-2 growth medium supplemented with EGM-2 bullet kit (Lonza) into a separate tube. Cells were spun at 300g for 5 min, diluted in 1 mL EGM-2 media and counted using a hemocytometer. 30,000-40,000 cells were plated on the 14 mm glass region of #1.5 glass-bottom dishes (Mat-Tek Corporation) coated with 10 µg/mL fibronectin (Fisher Scientific, CB-40008A). Media was changed after 2h and every 48h until imaging experiments. Cells were grown in a 5% CO_2 incubator at 37ºC for at least 72h prior to imaging.

Imaging Piezo1-tdTomato

Mobility of native Piezo1-tdTomato channels was imaged using Total Internal Reflection Fluorescence (TIRF) microscopy at 37°C. Piezo1-tdTomato MEFs and mLSECs were washed with phenol red-free DMEM/F12 (Invitrogen, 25116001) thrice and incubated in imaging solution, composed of 148 mM NaCl, 3 mM $CaCl_2$, 1 mM KCl, 2 mM $MgCl_2$, 8 mM Glucose, 10 mM HEPES, pH 7.30, and 316 mOsm/L osmolarity for 5 min. An Olympus IX83 microscope fitted with a 4-line cellTIRF illuminator, an environmental control enclosure and stage top incubator (Tokai Hit), and a PLAPO 60x oil immersion objective NA 1.45 was used to image cells. A programmable motorized stage (ASI) was used to identify samples throughout imaging. Images were acquired using the open source software µ-Manager (29). Cells were illuminated with a 561 nm laser and images were acquired using a Hamamatsu Flash 4.0 v2+ scientific CMOS camera at a frame rate of 10 frames/second with a 100 ms exposure time.

Piezo1-tdTomato cells (MEFs) were fixed using a 4% paraformaldehyde (Electron Microscopy Sciences, 15710), 1x PBS, 5 mM $MgCl_2$, 10 mM EGTA, 40 mg/mL sucrose buffer for 10 min at room temperature. The cells were washed thrice with PBS for 5 minutes.

Drug Treatment

Methyl-β-cyclodextrin-treated cells were incubated in 10 mM methyl-β-cyclodextrin (Sigma-Aldrich, C4555-5G) for 15 min before imaging. Cholesterol-MBCD-treated cells were incubated in 100 µg/mL cholesterol-water soluble, containing methyl-β-cyclodextrin (Sigma-Aldrich, C4951-30mg) and were incubated for 1 hour. Cells treated with 150 µM margaric acid (NuChek N-17-A) were incubated overnight at 37°C for 24h. Cells treated with 4 µM Yoda1 (Tocris 558610) or 4 µM GsMTx-4 (Tocris 4912) were incubated for 15 min. Margaric acid and Yoda1 were dissolved in Dimethyl sulfoxide (DMSO, Sigma Aldrich 276855-100ML). As such, DMSO was used as a control for margaric acid and Yoda1. All cells were imaged for 30 min post-treatment as described above.

Piezo1-tdTomato Trajectory Generation

Single particle tracking of Piezo1-tdTomato puncta was done using the open-source image processing and analysis program Flika (30). A difference of Gaussians algorithm was used as a spatial bandpass filter on the image stacks to detect the Piezo1-tdTomato punctae. The resulting enhanced stack was then thresholded using a manually selected threshold value to generate a binary image stack. Spatially-continuous pixels above this threshold were considered a single particle. A two-dimensional Gaussian function was used to determine the centroid of each particle to subpixel precision. Particles within three pixels of consecutive frames were assumed to represent the same Piezo1-tdTomato puncta. These particles were then linked to generate trajectories. Skipped frames were handled by inserting a placeholder value (numpy.nan) for missing coordinates (25, 31). A conversion factor equivalent to the length of a single pixel, 0.1092 µm, was used to transform two-dimensional coordinates in pixel units to microns. We limited our analysis to trajectories that were at least 20 seconds in length, which at a frame rate of 100 milliseconds, guaranteed a minimum of 200 positions per trajectory.

Trajectory Feature Selection and Analysis

A precursory scan of plotted trajectories from untreated MEFs revealed three visually distinct trajectory types: trajectories with a large extent ("mobile"), those with a very tight puncta ("trapped"), and trajectories that appeared to be between these two categories ("intermediate"). The large size of the trajectory data sets prompted us to develop a workflow for automated classification using supervised learning (32). The task of supervised learning is finding a model that maps input variables to an output variable based on paired input-output observations. In the context of classification, the output variable is a discrete set of classes, the input variables are termed *features* and the input-output pairs are termed the *training set* (32).

In the context of classification of SPT trajectories using supervised learning methods, a trajectory feature is generated by mapping the trajectory's spatial coordinates to a single scalar that is invariant to rigid-body motions of the entire trajectory (33). Among the trajectory features reported in the literature (33, 34), we only considered those that described geometric aspects of the trajectories.

To further examine each one of the candidate features, we classified a set of 1,000 trajectories of Piezo1-tdTomato untreated MEFs by visual inspection (as described in the next section), we then mapped each trajectory onto the feature under examination, and checked whether the corresponding feature distribution was partitioned by our classification scheme (see Supplementary Fig.1). Following this approach, we selected six features: net displacement, straightness, radius of gyration, asymmetry, kurtosis, and fractal dimension, which are described in detail in the Supplemental Information.

Each one of the six selected features computed over the 1,000-trajectory data set was normalized using a Box-Cox transformation (35). A principal component analysis was performed on the transformed data set of six-dimensional vectors. Nearly 90% of the variance was explained by the first three principal components. The projection of the transformed data set on this reduced three-dimensional principal component subspace was used as the training set for the classification.

All feature calculations and analyses were carried out with in-house Python scripts using the Numpy (31), SciPy (36), and Pandas (37) libraries. Data visualization was performed with Matplotlib (38) and seaborn (39).

Trajectory Labeling

The 1,000 trajectories randomly sampled from the 11,794 trajectories of Piezo1-tdTomato untreated MEFs indicated above were visually classified (labeled) as "mobile", "trapped", or "intermediate" by three different researchers. This was a blind process where each researcher independently performed their own labeling, without knowledge or influence from the other parties. Through this process, each of the 1,000 trajectories was assigned three possible labels, from which the majority label was chosen as the final class for each trajectory. This three-party labeling process was an effort to reduce bias in the initial subjective classification.

Support Vector Machine Training

A support vector machine (SVM) is a supervised learning algorithm designed to maximize the margin of separation between sets of features with different labels by identifying dividing hyperplanes. The features in this context are nonlinear transformations of the original observations performed with one of several so-called kernel functions. Kernel functions have adjustable parameters that are usually chosen by performing a search over the parameter space, performing a cross-validation with the training set on each specific choice of parameters, and selecting the one with the highest accuracy. Here, the Radial Basis Function (RBF, a Gaussian function) was chosen as kernel function. An SVM with an RBF kernel has two tunable parameters, a regularization parameter, C, and a curvature or shape parameter, γ, which were selected based on a six-fold cross-validation carried out via grid search of the parameter space. Briefly, the training set was split 80:20 for training and testing/validation. For each point in the grid, the SVM was trained on the same 80% of training data, and then evaluated against the remaining 20% via cross-validation. For cross-validation, the 20% hold out set was randomly split into 6 subsets and then stratified to balance class representations in each set. The SVM performance was evaluated and averaged for all 6 subsets and compared across all grid search configurations with the best parameters determined by the highest F1-score averaged over the three classes. The F1-score is a measure of a binary classifier's accuracy, defined as the harmonic mean of the classifier's *precision* and *recall*. Precision is the total number of correctly predicted observations divided by the total number of predictions. Recall is the total number of correctly predicted observations divided by the total number of observations. The final values of $C = 4\ 0.0$ and $\gamma = 0.03$ were chosen, corresponding to an average F1-score of 87% (Supplementary Fig.7). The was SVM implemented with in-house Python scripts, using the Numpy (31), Pandas (37) and Scikit-Learn (40) libraries. The training set split was performed using the test-train-split module in the Scikit-learn library. Confusion matrices for the test and train portions, along with table of accuracy metrics are available in the Supplementary Information.

RESULTS

Piezo1-tdTomato puncta exhibit heterogeneous mobility

We imaged with TIRFM endogenously expressed Piezo1-tdTomato in mouse embryonic fibroblast cells (MEFs) harvested from Piezo1-tdTomato reporter mice. Piezo1 channels were visible as distinct puncta as described earlier (25) but with higher fidelity due to improvements in camera technology (Fig. 1A). Visual inspection of videos collected revealed that some puncta were quite mobile while others showed little or no mobility (Fig. 1A and Supplemental Video 1 in Supplementary Material). The reduced mobility of some Piezo1 puncta was particularly evident in regions of the cell where Piezo1 puncta appeared to cluster together in structures reminiscent of focal adhesions (Fig. 1A, green inset; also compare green and blue insets in Supplemental Video 1), in agreement with reports that Piezo1 is enriched at focal adhesions under certain conditions (41, 42). We examined the Piezo1 trajectories more closely and found that they could be classified into three categories by visual inspection of their two-dimensional extent: "mobile," where trajectories exhibit a large extent, "trapped," where trajectories are limited to a very small area, and "intermediate," where trajectories are in-between the other two categories (Fig.1B).

We were able to consistently classify 1,000 trajectories by visual inspection, but manual classification would be impractical to classify the entire SPT data set of 86,432 trajectories. This motivated the implementation of an algorithmic method for unbiased classification. A number of geometric features have been proposed for automating the classification of trajectories derived from SPT data (33, 34). We chose a set of six features (net displacement, straightness, radius of gyration, asymmetry, fractal dimension, and kurtosis that are defined in the Supplemental Information). This set of features was able to segregate an initial subset of 1,000-trajectories in a manner consistent with the classification by visual inspection (see Supplementary Fig.1).

When computed over the initial 1,000-trajectory data set, the six features exhibited various degrees of pairwise correlation (see Supplementary Fig.1), suggesting that additional dimensionality reduction steps were needed. We performed a principal component analysis (PCA) on the six-dimensional feature vectors encoding the 1000-trajectory data set and found that the first three principal components accounted for nearly 90% of the total variance with the first principal component accounting for more than 60% of the total variance (see Supplementary Fig.2).

Projecting the six-dimensional feature vectors onto the reduced space of the first three principal components separates the classes assigned by visual inspection, primarily along the first principal component (see Fig.2A and Supplementary Fig.3, where the 1000-trajectory data are represented as dots). Consistent with this result, three features directly associated to the trajectory spread (net displacement, radius of gyration, and fractal dimension), dominate the first principal component (see Fig.2A and Supplementary Fig.3, where the individual features are represented as vector arrows). However, the class separation along the first principal component is not without overlaps (see Fig.2A). To define boundaries between classes in this three-dimensional subspace, we trained an SVM classifier using the projected features vectors of the visually-classified 1,000-trajectory data set. (Fig.2B and Supplementary Fig.3).

To validate our classification approach, we performed a control experiment with paraformaldehyde-treated fixed cells, in which Piezo1-tdTomato puncta are rendered immobile. We used the SVM classifier to evaluate the trajectories resulting from the corresponding SPT analysis of these fixed cells. Consistent with the experimental treatment, we found that over 99% of these trajectories were classified as "trapped" with the remainder classified as "intermediate" (see Fig.2C and Supplementary Fig.4). Furthermore, analysis of Piezo1-tdTomato trajectories obtained from a different cell type, mouse liver sinusoidal endothelial cells (mLSECs), exhibited the three classes seen for MEFs (Fig.2C), suggesting that the observed heterogeneity is not limited to Piezo1-tdTomato expressed in MEFs.

Manipulation of the lipid membrane and modulation of channel activity reveals shifts in Piezo1 mobility

Previous studies have shown that changes to membrane composition can affect membrane protein diffusion (26, 43–45). In order to explore the relationship between membrane composition and Piezo1 mobility, we used chemical agents to manipulate the membrane in MEFs.

We treated MEFs with 10 mM MBCD for 15 minutes in order to deplete cholesterol from the membrane and acquired Piezo1-tdTomato TIRFM videos. We then generated and classified Piezo1-tdTomato trajectories from these videos as described above. When we compared the Piezo1-tdTomato trajectories from MBCD-treated cells to those from untreated control cells, MBCD-treated MEFs had a higher proportion of "mobile" trajectories (Supplementary Fig.5A). To quantify the effect of the MBCD treatment on the mobility of Piezo1 puncta, we use the trajectory's radius of gyration, R_g, one of the dominant features in the classification (Fig.2 and Supplementary Fig.3A), defined as

$$R_g^2 = \frac{1}{N}\sum_{i=1}^{N}(\vec{x}_i - \langle\vec{x}\rangle)^2 \tag{1}$$

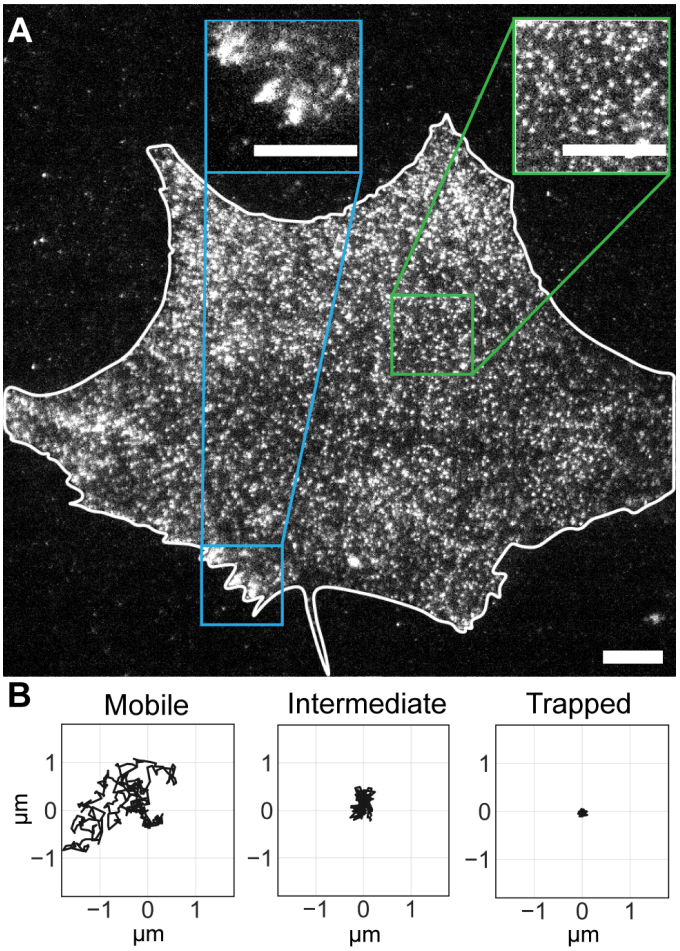

Figure 1: TIRF microscopy and single particle tracking reveals heterogeneity in Piezo1-tdTomato mobility. A. Representative fluorescence image of Piezo1-tdTomato puncta in live MEFs harvested from Piezo1-tdTomato reporter mice using TIRFM. The white line denotes the cell boundary. Insets show enlarged regions of interest. B. The trajectories generated from the single particle tracking analysis can be classified by visual inspection into three different classes: those that showed high mobility were nominally identified as "mobile," those exhibiting very small displacements as "trapped," and trajectories with limited spread that were deemed not to belong to either of those categories were labeled "intermediate." See also Supplemental Video 2 in Supplementary Material.
Scale bars = 10 µm.

where $\vec{x}_i$ is the particle's position at the i-th point of the trajectory, N is the total number of trajectory points, and $\langle\vec{x}\rangle$ is the mean position. To account for variability in step lengths across different trajectories, we scaled R_g by the trajectory's mean step length, $\langle s\rangle = \frac{1}{N-1}\sum_{i=1}^{N-1}|\vec{x}_{i+1}-\vec{x}_i|$, where $|\vec{x}_{i+1}-\vec{x}_i|$ is the Euclidean distance between two consecutive points of the trajectory (see Supplemental Information for details). The resulting scaled R_g ($R_g/\langle s\rangle$) can be used as a consistent measure of trajectory spread.

Compared to the untreated control, application of MBCD increased the scaled R_g of Piezo1 "mobile" trajectories (Fig.3), suggesting that cholesterol depletion increases Piezo1 puncta mobility. To determine how the inverse – increasing cholesterol content of the membrane – affects puncta diffusion, we supplemented MEFs with 100 µg/mL cholesterol-MBCD for 1 hour. Utilizing the same methods that we applied to MBCD-treated MEFs, we compared trajectories from untreated control cells to those supplemented with cholesterol-MBCD, and found that cholesterol-MBCD treatment resulted in a lower proportion of mobile trajectories (Supplementary Fig.5B). Similarly, the scaled radius of gyration for cholesterol-MBCD-treated "mobile" Piezo1 trajectories decreased compared to untreated control (Fig.3), suggesting that the Piezo1 puncta mobility decreases when cholesterol is increased in the membrane.

Cholesterol supplementation stiffens the membrane, and we next investigated how membrane stiffening through other

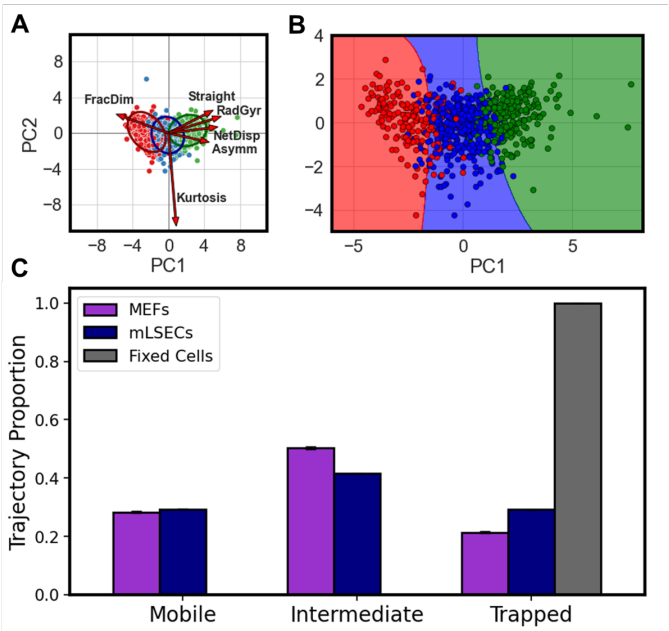

Figure 2: Machine-learning methodologies are used to automate the classification of Piezo 1 trajectories. Visual inspection of 1,000 trajectories led us to partition the trajectories into three classes: “mobile", “intermediate", and “trapped". We characterized these 1,000 trajectories using six geometric features, and carried out a principal component analysis to determine a reduced subspace suitable for training a supervised learning algorithm (SVM) for automated sorting of tens of thousands of trajectories into the three classes identified by visual inspection. A. Principal component analysis biplot of a set of Piezo1 trajectories encoded as six-dimensional geometric feature vectors and classified by visual inspection. The 1,000 observations are shown as dots colored by class (“mobile,” green; “intermediate,” blue; “trapped”, red). The three classes are largely separated along the first principal component (PC1) into three overlapping groups, as evidenced by the 95% confidence ellipses for each class. Out of the six geometric features used to describe the trajectories (shown as red arrows), the largest contributions to PC1 are from net displacement, radius of gyration, and fractal dimension, all of which characterize the trajectory spread (see also Supplementary Fig.3) B. The set of 1000 trajectories classified by visual inspection was used to train a SVM classifier on the subspace of the feature vectors’ first three principal components. The partition of the PC1-PC2 subspace by the SVM is identified by the background colors in this version of the 1000-trajectory training set scatter plot. C. The automated classification of Piezo1-tdTomato trajectories from mouse embryonic fibroblasts (MEFs, purple) and mouse liver sinusoidal endothelial cells (mLSECs, blue) both show distribution into the three classes “mobile,” “intermediate,” and “trapped”, suggesting that the observed heterogeneity is not restricted to MEF cells. Almost all the trajectories in a SPT data set from MEFs fixed with paraformaldehyde (gray), containing immobile Piezo1-tdTomato, are identified as “trapped”.

agents affects diffusion. We incubated cells for 24 hours in 150 µM margaric acid, a fatty acid known to stiffen the membrane (46). We then compared the margaric acid-treated trajectories to the DMSO-treated control trajectories and found that, like cholesterol-MBCD treatment, margaric acid decreased the proportion of “mobile” trajectories (Supplementary Fig.5C), albeit to a lesser extent. Similarly, the scaled R_g of margaric acid-treated Piezo1 “mobile” trajectories decreased compared to the DMSO-treated control (Fig.3). Interestingly, margaric acid is also known to inhibit Piezo1 activity (46). To explore whether Piezo1’s activation state may also affect its mobility, we next examined the effect of drugs that modulate Piezo1 activity.

GsMTx-4, a spider venom-derived peptide, blocks cation-selective stretch-activated channels and has been shown to inhibit Piezo1 activity (47). We incubated MEFs in 4 µM GsMTx-4 for 15 min to inhibit Piezo1 channels. We found that the proportion of “mobile” GsMTx-4-treated Piezo1-tdTomato trajectories was lower than the untreated control cells (Supplementary Fig.5D). The scaled R_g of GsMTx-4 treated puncta was also decreased compared to that of the untreated control (Fig.3). Thus, inhibition of Piezo1 appears to reduce its mobility.

We next examined the effect of Yoda1, a chemical activator of Piezo1, on mobility. We imaged cells treated with 4 µM Yoda1 for 15 minutes, and found that the proportion of “mobile” Piezo1 puncta was greater than those treated with DMSO (Supplementary Fig.5E). Yoda1-treated Piezo1 also exhibited higher scaled R_g than the DMSO-treated control (Fig.3), further suggesting that active channels are more mobile. Together, these results indicate that the diffusion of the Piezo1-tdTomato

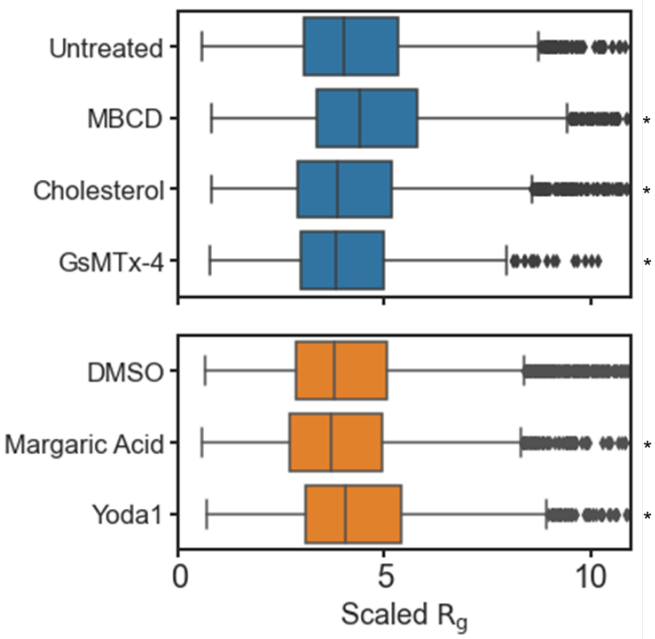

Figure 3: "Mobile" Piezo1-tdTomato exhibits changes in trajectory spread consistent with perturbations to membrane composition and channel activity. (*top*) 10 mM methyl-β-cyclodextrin (MBCD), 100 µg/mL cholesterol and 4 µM GsMTx-4 compared to untreated MEFs as control. (*bottom*) 150 µM margaric acid and 4 µM Yoda1 compared to DMSO-treated MEFs as control. All treatments affecting membrane composition or channel activity induce statistical significant changes in the distribution of the scaled R_g in a two-sample Kolmogorov-Smirnov test relative to the corresponding control (* $p < 0.05$).

mobile class is sensitive to changes in membrane composition as well as to the activation state of the Piezo1 channel.

The mobile class is subdiffusive

The available evidence from fluorescence correlation spectroscopy, fluorescent recovery after photobleaching, and SPT indicates that Brownian motion is not the prevalent diffusive behavior of proteins in the membrane environment (reviewed in (28, 48, 49)). Although the mechanistic details of Piezo1 diffusion in the plasma membrane have yet to be elucidated, the underlying assumption made so far in the literature is that Piezo1 diffusion can be described as Brownian motion (26, 50). With the tagged particle's trajectory denoted as $\vec{x}(t)$, diffusive behavior can be characterized by the so-called time averaged mean squared displacement (TAMSD) (49)

$$\overline{\delta^2(\Delta)} = \frac{1}{T-\Delta}\int_0^{T-\Delta} (\vec{x}(t+\Delta) - \vec{x}(t))^2 dt \tag{2}$$

where T is the trajectory's total length in time and Δ is the lag time.

Unrestricted Brownian motion is characterized by a linear time dependence of the TAMSD

$$\overline{\delta^2(\Delta)} = K\Delta \tag{3}$$

where K is a constant. Deviations from this linear behavior, termed anomalous diffusion, are commonly observed in SPT experiments and modeled using a power-law form

$$\overline{\delta^2(\Delta)} = K_\alpha \Delta^\alpha \tag{4}$$

where α, the so-called anomalous exponent, is a positive real constant. A time dependence of the TAMSD that is slower than linear ($0 < \alpha < 1$) is called subdiffusion, while a time dependence that is faster than linear ($\alpha > 1$) is called superdiffusion.

We computed the TAMSD of the individual Piezo1 trajectories in the "mobile" class (see Fig.4A). Fitting the individual TAMSDs to a power law (Eq. 4) yields a broad distribution of anomalous diffusion exponents, α (Fig.4B). Similar results were

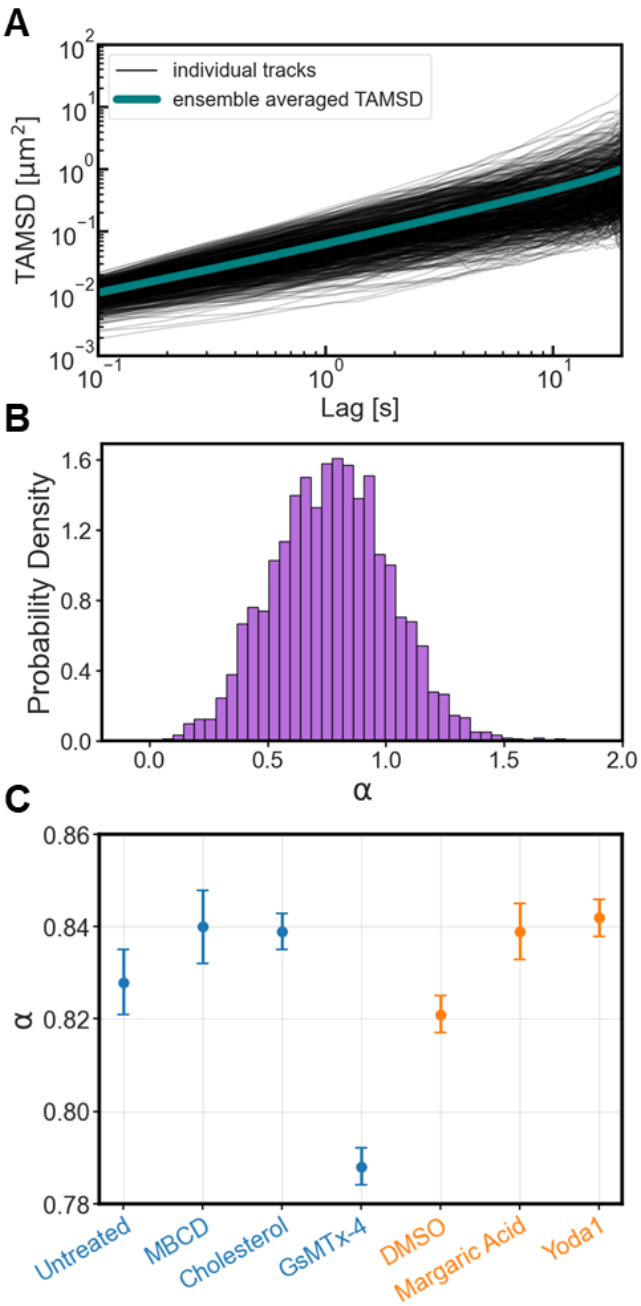

Figure 4: "Mobile" Piezo1-tdTomato trajectories are heterogeneous and exhibit anomalous subdiffusion. A. TAMSD as a function of lag time of Piezo1-tdTomato expressed in MEFs (individual trajectories, black; ensemble average, green). Only the untreated condition is shown here; similar results for all tested conditions are shown in Supporting Fig.6). B. The corresponding anomalous exponents from individual Piezo1-tdTomato trajectories are broadly distributed. C. The mean estimates of the anomalous exponent distributions indicate subdiffusive behavior across all tested conditions. Line ranges are 95% confidence intervals. The mean estimates from all treatments are different from their corresponding control at this confidence level (blue, treatments using untreated MEFs as control; orange, treatments using DMSO-treated MEFs as control).

observed across all the conditions reported in the previous section (Supplementary Fig.6). These results are not unexpected. SPT is a time limited recording of a stochastic process. Therefore, estimates of the anomalous diffusion exponent may vary significantly among trajectories collected from the same experiment. A common practice is to perform an additional average of

the TAMSD over an ensemble of N collected trajectories,

$$\langle \overline{\delta^2(\Delta)} \rangle = \sum_{i=1}^{N} \overline{\delta_i^2(\Delta)}. \tag{5}$$

The resulting ensemble-averaged TAMSD (EA-TAMSD) (shown as green traces in Fig.4A and Supplementary Fig.6) is sufficient to eliminate the variability associated with time limited measurements and random errors, but it fails to account for measurement noise as well as the intrinsic variability in the particles' diffusing behavior (51, 52). Accurate estimates of the mean and width of the distribution of anomalous exponents for the ensemble of particles can be obtained from the EA-TAMSD after correcting for these systematic errors as described in (51). The results for the Piezo1 "mobile" class indicate a consistent subdiffusive behavior across all the experimental conditions (see Fig.4C).

In contrast to the trajectory spread analysis reported in (Fig.3), where changes to the scaled R_g distribution can be directly associated to changes in Piezo1 mobility upon membrane composition and channel activation state perturbations, an interpretation of the small but statistically significant changes to the anomalous exponent would require a detailed modeling of the diffusion mechanisms, which is beyond the scope of the present TAMSD analysis. Nevertheless, the persistence of alpha well below unity indicates that anomalous diffusion is a consistent property of Piezo1 mobility under a variety of conditions.

DISCUSSION

Here, we follow up on our previous finding that Piezo1 channels are mobile (25) by performing single-particle tracking (SPT) of endogenously expressed Piezo1-tdTomato channel puncta. We observed that Piezo1 exhibits multiple modes of diffusion in two different cell types, MEFs and mLSECs. Through visual observation of the trajectories, we classified the trajectories into three classes based on their spatial extent - "mobile", "intermediate" and "trapped." We then implemented a supervised machine approach algorithm to automate this classification for thousands of trajectories, and examined the effect of specific pharmacological perturbations on Piezo1 mobility.

Our findings are consistent with a large body of experimental evidence indicating that the lateral motion of membrane proteins in the complex environment of the plasma membrane is dependent on the local structure and regulatory signals encountered by each individual protein or cluster of proteins (28, 53, 54). This behavior is put in full display by the spatiotemporal resolution of SPT of tagged proteins (54, 55). Trajectory classification is thus a prerequisite for the interpretation of the Piezo1 SPT data.

Almost all of the schemes proposed in the literature for the classification of SPT trajectories of membrane proteins are based on descriptions of the motion itself or on more detailed diffusion models (56–65). We have taken an approach to trajectory classification that relies only on geometrical aspects of the trajectories without input from diffusion models at any level of the classification process. A similar approach was proposed recently by Pinholt et al. and shown to effectively identify distinct diffusion modes in a wide variety of systems (66). In contrast to Pinholt et al., our set of descriptive features for classification does not include quantities associated with the MSD analysis of the trajectory. By separating the trajectory classification from the description of the underlying diffusive process, we can in the future interrogate each class separately using experimental methods to probe specific connections between channel activity and mobility and use diffusion models in the interpretation of those results. Here, we have begun to address the first part of this program, by developing a reliable automated classification scheme.

According to our classification scheme, a class of trajectories nominally identified as "mobile" exhibit high mobility in the plasma membrane compared to the other two classes, "trapped" or "intermediate." A recent pre-print by Vaisey et al. reporting SPT on endogenous Piezo1 in red blood cells also observed heterogeneity in Piezo1 trajectories (50). Our detailed analysis of this class suggests that Piezo1 mobility is sensitive to changes in membrane composition and that activity may modulate the channel's diffusion. Supplementation of the membrane with cholesterol or margaric acid decreases Piezo1 mobility, while cholesterol depletion via MBCD increases mobility. These results are consistent with findings from several ion channel diffusion studies. Removal of membrane cholesterol reduces the population of confined Orai1, an ion channel that causes extracellular calcium influx upon internal calcium store depletion, and causes the channels to move in a linear pattern (44). Similarly, both serotonin transporters (67) and dopamine transporters (68) increase in lateral mobility following MBCD treatment. Ridone *et al.* also found that cholesterol depletion increased the diffusion of overexpressed Piezo1 in HEK293T cells (26).

Our results demonstrate that drug-induced changes to the channel state affect channel mobility in MEFs. Margaric acid has been shown to stiffen the plasma membrane and inhibit Piezo1 activation. When we treated cells with margaric acid, Piezo1-tdTomato trajectories were less mobile than DMSO-treated control trajectories. Romero et al. had previously proposed that margaric acid's inhibitory effect on Piezo1 could be a result of the drug's role in membrane remodeling (46). Another channel inhibitor that partitions into the membrane, the amphipathic tarantula venom peptide, GsMTx-4 (47), has been posited

to disrupt transfer of force to the channel in the plasma membrane, thereby inhibit Piezo1 activation (69). While GsMTx-4 treatment results in a decrease in mobility relative to the untreated control, suggesting that closed channels may be less mobile, the observed shifts in mobility could also be a result of potential shifts in local membrane tension rather than channel conformational changes. Conversely, we have shown that Yoda1, a Piezo1 agonist (70), increases mobility. However, it is important to note that while Yoda1 activates the Piezo1 channel and results in greater mobility, chemically-driven activation by Yoda1 may not necessarily be analogous to the behavior of channels activated by an increase in local membrane tension. Yoda1 has been shown to stabilize the open state (70, 71), and it has been proposed that Yoda1 acts as a molecular wedge when bound to Piezo1, affecting both the channel's mechanosensitivity and flexibility of the blades (72). It is unknown whether this steric modification may be enough to affect channel diffusion. Future studies simultaneously monitoring the activity and mobility of Piezo1 are needed.

Our MSD analysis of the "mobile" class of Piezo1 revealed a consistent subdiffusive behavior across all experimental conditions, suggesting that this may be a fundamental characteristic of Piezo1 mobility in the plasma membrane. Although the underlying physical mechanisms may vary, a wealth of experimental evidence suggests that subdiffusion is a ubiquitous mode of motion for submicron particles in the cell membrane (28, 48, 49, 59, 60, 73). Subdiffusion may be the result of the lateral heterogeneity of the membrane environment sampled by the channel or it may reflect transient associations with other membrane components (28, 54, 74). Specific hypotheses in the case of Piezo1 will require detailed modeling of the diffusion process, which is the subject of a future study.

Piezo1 mobility has several important implications. Channel mobility may allow fewer channels to explore a larger domain of the cell to efficiently transduce mechanical forces. Mobility may also function as a mechanism for channels to dynamically adjust the cellular response to mechanical forces. Mechanical forces can act upon a cell at any time, from anywhere, and Piezo1's mobility in conjunction with its activation state may aid the cell in adjusting to these responses. Additionally, open and closed channels may exhibit different mobilities, providing specific mechanisms through which the cell can modulate mechanotransduction. For instance, closed channels may be more mobile than open channels. This would allow closed channels to explore the cell in search of mechanical cues, and for open channels to linger at cellular regions experiencing mechanical stimuli. Conversely, open channels may be more mobile than closed channels. In this case, when the channel experiences mechanical forces, open-mobile channels may move away from persistent mechanical stimuli, thereby closing the channel and terminating the mechanotransduction. Our findings set the stage for future work examining Piezo1 mobility in the context of channel activity.

AUTHOR CONTRIBUTIONS

M.M.P. and D.J.T. conceptualized the research. A.T.L., V.T., J.A.F., G.A.B, E.L.E. were involved with the methodology. A.T.L., V.T. were responsible for data curation, investigation, formal analysis, and validation. M.M.P. and D.J.T. were responsible for overseeing the project, and for funding acquisition and resources. A.T.L., V.T., J.A.F, D.J.T., and M.M.P wrote the manuscript. The co-first authorship order was determined via a coin flip; both A.T.L. and V.T. contributed equally and have the right to list their name first in their CV. All authors reviewed and edited the manuscript.

ACKNOWLEDGMENTS

We thank Dr. Ardem Patapoutian for the gift of the Piezo1-tdTomato mice, Michael Thanh-Phong Vu for assistance with trajectory generation from TIRFM videos, and the Pathak and Tobias groups for invaluable discussions. This work utilized computing resources operated by the Research Cyberinfrastructure Center at the University of California, Irvine.

FUNDING

This work was supported by an NIH grant R01NS109810 to M.M.P and R01EY031587 to D.J.T. A.T.L. was supported by the R01 (NS10981) Diversity Supplement and NIH F31 1F31NS127594-0.

REFERENCES

1. Coste, B., J. Mathur, M. Schmidt, T. J. Earley, S. Ranade, M. J. Petrus, A. E. Dubin, and A. Patapoutian, 2010. Piezo1 and Piezo2 Are Essential Components of Distinct Mechanically Activated Cation Channels. *Science* 330:55–60.

2. Ranade, S. S., Z. Qiu, S.-H. Woo, S. S. Hur, S. E. Murthy, S. M. Cahalan, J. Xu, J. Mathur, M. Bandell, B. Coste, Y.-S. J. Li, S. Chien, and A. Patapoutian, 2014. Piezo1, a mechanically activated ion channel, is required for vascular development in mice. *Proc. Natl. Acad. Sci. U.S.A.* 111:10347–10352.

3. Li, J., B. Hou, S. Tumova, K. Muraki, A. Bruns, M. J. Ludlow, A. Sedo, A. J. Hyman, L. McKeown, R. S. Young, N. Y. Yoldasheva, Y. Majeed, L. A. Wilson, B. Rode, M. A. Bailey, H. R. Kim, Z. Fu, D. A. L. Carter, J. Bilton, H. Imrie, P. Ajuh, T. N. Dear, R. M. Cubbon, M. T. Kearney, K. R. Prasad, P. C. Evans, J. F. X. Ainscough, and D. J. Beech, 2014. Piezo1 integration of vascular architecture with physiological force. *Nature* 515:279–282.

4. Nonomura, K., V. Lukacs, D. T. Sweet, L. M. Goddard, A. Kanie, T. Whitwam, S. S. Ranade, T. Fujimori, M. L. Kahn, and A. Patapoutian, 2018. Mechanically activated ion channel PIEZO1 is required for lymphatic valve formation. *Proc. Natl. Acad. Sci. U.S.A.* 115:12817–12822.

5. Sun, W., S. Chi, Y. Li, S. Ling, Y. Tan, Y. Xu, F. Jiang, J. Li, C. Liu, G. Zhong, D. Cao, X. Jin, D. Zhao, X. Gao, Z. Liu, B. Xiao, and Y. Li, 2019. The mechanosensitive Piezo1 channel is required for bone formation. *eLife* 8:e47454.

6. Zeng, W.-Z., K. L. Marshall, S. Min, I. Daou, M. W. Chapleau, F. M. Abboud, S. D. Liberles, and A. Patapoutian, 2018. PIEZOs mediate neuronal sensing of blood pressure and the baroreceptor reflex. *Science* 362:464–467.

7. Hill, R. Z., M. C. Loud, A. E. Dubin, B. Peet, and A. Patapoutian, 2022. PIEZO1 transduces mechanical itch in mice. *Nature* 607:104–110.

8. Ranade, S. S., S.-H. Woo, A. E. Dubin, R. A. Moshourab, C. Wetzel, M. Petrus, J. Mathur, V. Bégay, B. Coste, J. Mainquist, A. J. Wilson, A. G. Francisco, K. Reddy, Z. Qiu, J. N. Wood, G. R. Lewin, and A. Patapoutian, 2014. Piezo2 is the major transducer of mechanical forces for touch sensation in mice. *Nature* 516:121–125.

9. Chesler, A. T., M. Szczot, D. Bharucha-Goebel, M. Čeko, S. Donkervoort, C. Laubacher, L. H. Hayes, K. Alter, C. Zampieri, C. Stanley, A. M. Innes, J. K. Mah, C. M. Grosmann, N. Bradley, D. Nguyen, A. R. Foley, C. E. Le Pichon, and C. G. Bönnemann, 2016. The Role of PIEZO2 in Human Mechanosensation. *N. Engl. J. Med.* 375:1355–1364.

10. Woo, S.-H., V. Lukacs, J. C. de Nooij, D. Zaytseva, C. R. Criddle, A. Francisco, T. M. Jessell, K. A. Wilkinson, and A. Patapoutian, 2015. Piezo2 is the principal mechanotransduction channel for proprioception. *Nat. Neurosci.* 18:1756–1762.

11. Szczot, M., J. Liljencrantz, N. Ghitani, A. Barik, R. Lam, J. H. Thompson, D. Bharucha-Goebel, D. Saade, A. Necaise, S. Donkervoort, A. R. Foley, T. Gordon, L. Case, M. C. Bushnell, C. G. Bönnemann, and A. T. Chesler, 2018. PIEZO2 mediates injury-induced tactile pain in mice and humans. *Sci. Transl. Med.* 10:eaat9892.

12. Murthy, S. E., M. C. Loud, I. Daou, K. L. Marshall, F. Schwaller, J. Kühnemund, A. G. Francisco, W. T. Keenan, A. E. Dubin, G. R. Lewin, and A. Patapoutian, 2018. The mechanosensitive ion channel Piezo2 mediates sensitivity to mechanical pain in mice. *Sci. Transl. Med.* 10:aat9897.

13. Holt, J. R., W.-Z. Zeng, E. L. Evans, S.-H. Woo, S. Ma, H. Abuwarda, M. Loud, A. Patapoutian, and M. M. Pathak, 2021. Spatiotemporal dynamics of PIEZO1 localization controls keratinocyte migration during wound healing. *eLife* 10:e65415.

14. Pathak, M. M., J. L. Nourse, T. Tran, J. Hwe, J. Arulmoli, D. T. T. Le, E. Bernardis, L. A. Flanagan, and F. Tombola, 2014. Stretch-activated ion channel Piezo1 directs lineage choice in human neural stem cells. *Proc. Natl. Acad. Sci. U.S.A.* 111:16148–16153.

15. Jankovsky, N., A. Caulier, J. Demagny, C. Guitton, S. Djordjevic, D. Lebon, H. Ouled-Haddou, V. Picard, and L. Garçon, 2021. Recent advances in the pathophysiology of PIEZO1-related hereditary xerocytosis. *Am. J. Hematol.* 96:1017–1026.

16. Lukacs, V., J. Mathur, R. Mao, P. Bayrak-Toydemir, M. Procter, S. M. Cahalan, H. J. Kim, M. Bandell, N. Longo, R. W. Day, D. A. Stevenson, A. Patapoutian, and B. L. Krock, 2015. Impaired PIEZO1 function in patients with a novel autosomal recessive congenital lymphatic dysplasia. *Nat. Comm.* 6:6:8329.

17. Saotome, K., S. E. Murthy, J. M. Kefauver, T. Whitwam, A. Patapoutian, and A. B. Ward, 2017. Structure of the mechanically activated ion channel Piezo1. *Nature* 554:481–486.

18. Ge, J., W. Li, Z. Qiancheng, N. Li, M. Chen, P. Zhi, R. Li, N. Gao, B. Xiao, and M. Yang, 2015. Architecture of the mammalian mechanosensitive Piezo1 channel. *Nature* 527:64–69.

19. Guo, Y. R., and R. MacKinnon, 2017. Structure-based membrane dome mechanism for Piezo mechanosensitivity. *eLife* 6:e33660.

20. Zhao, Q., H. Zhou, S. Chi, Y. Wang, J. Wang, J. Geng, K. Wu, W. Liu, T. Zhang, M.-Q. Dong, J. Wang, X. Li, and B. Xiao, 2018. Structure and mechanogating mechanism of the Piezo1 channel. *Nature* 554:487–492.

21. Haselwandter, C. A., and R. MacKinnon, 2018. Piezo's membrane footprint and its contribution to mechanosensitivity. *eLife* 7:e41968.

22. Lewis, A. H., and J. Grandl, 2015. Mechanical sensitivity of Piezo1 ion channels can be tuned by cellular membrane tension. *eLife* 4:e12088.

23. Syeda, R., M. N. Florendo, C. D. Cox, J. M. Kefauver, J. S. Santos, B. Martinac, and A. Patapoutian, 2016. Piezo1 Channels Are Inherently Mechanosensitive. *Cell Rep.* 17:1739–1746.

24. Cox, C. D., C. Bae, L. Ziegler, S. Hartley, V. Nikolova-Krstevski, P. R. Rohde, C.-A. Ng, F. Sachs, P. A. Gottlieb, and B. Martinac, 2016. Removal of the mechanoprotective influence of the cytoskeleton reveals PIEZO1 is gated by bilayer tension. *Nat. Commun.* 7:10366.

25. Ellefsen, K. L., J. R. Holt, A. C. Chang, J. L. Nourse, J. Arulmoli, A. H. Mekhdjian, H. Abuwarda, F. Tombola, L. A. Flanagan, A. R. Dunn, I. Parker, and M. M. Pathak, 2019. Myosin-II mediated traction forces evoke localized Piezo1-dependent Ca2 flickers. *Commun. Biol.* 2:298.

26. Ridone, P., E. Pandzic, M. Vassalli, C. D. Cox, A. Macmillan, P. A. Gottlieb, and B. Martinac, 2020. Disruption of membrane cholesterol organization impairs the activity of PIEZO1 channel clusters. *J. Gen. Physiol.* 152:e201912515.

27. Sezgin, E., I. Levental, S. Mayor, and C. Eggeling, 2017. The mystery of membrane organization: composition, regulation and roles of lipid rafts. *Nat. Rev. Mol. Cell Biol.* 18:361–374.

28. Jacobson, K., P. Liu, and B. C. Lagerholm, 2019. The Lateral Organization and Mobility of Plasma Membrane Components. *Cell* 177:806–819.

29. Edelstein, A., N. Amodaj, K. Hoover, R. Vale, and N. Stuurman, 2010. Computer Control of Microscopes Using μManager. *Curr. Protoc. Mol. Biol.* 92:14.20.1—14.20.17.

30. Ellefsen, K. L., B. Settle, I. Parker, and I. F. Smith, 2014. An algorithm for automated detection, localization and measurement of local calcium signals from camera-based imaging. *Cell Calcium* 56:147–156.

31. Harris, C. R., K. J. Millman, S. J. van der Walt, R. Gommers, P. Virtanen, D. Cournapeau, E. Wieser, J. Taylor, S. Berg, N. J. Smith, R. Kern, M. Picus, S. Hoyer, M. H. van Kerkwijk, M. Brett, A. Haldane, J. F. del Río, M. Wiebe, P. Peterson, P. Gérard-Marchant, K. Sheppard, T. Reddy, W. Weckesser, H. Abbasi, C. Gohlke, and T. E. Oliphant, 2020. Array programming with NumPy. *Nature* 585:357–362.

32. James, G., D. Witten, T. Hastie, and R. Tibshirani, 2021. Statistical Learning. *In* Springer Texts in Statistics, Springer US, 15–57.

33. Helmuth, J. A., C. J. Burckhardt, P. Koumoutsakos, U. F. Greber, and I. F. Sbalzarini, 2007. A novel supervised trajectory segmentation algorithm identifies distinct types of human adenovirus motion in host cells. *J. Struct. Biol.* 159:347–358.

34. Wagner, T., A. Kroll, C. R. Haramagatti, H. G. Lipinski, and M. Wiemann, 2017. Classification and segmentation of nanoparticle diffusion trajectories in cellular micro environments. *PLoS ONE* 12:e0170165.

35. Box, G. E. P., and D. R. Cox, 1964. An Analysis of Transformations. *J. R. Stat. Soc. Series B Stat. Methodol.* 26:211–243.

36. Virtanen, P., R. Gommers, T. E. Oliphant, M. Haberland, T. Reddy, D. Cournapeau, E. Burovski, P. Peterson, W. Weckesser, J. Bright, S. J. van der Walt, M. Brett, J. Wilson, K. J. Millman, N. Mayorov, A. R. J. Nelson, E. Jones, R. Kern, E. Larson, C. J. Carey, İ. Polat, Y. Feng, E. W. Moore, J. VanderPlas, D. Laxalde, J. Perktold, R. Cimrman, I. Henriksen, E. A. Quintero, C. R. Harris, A. M. Archibald, A. H. Ribeiro, F. Pedregosa, P. van Mulbregt, and SciPy 1.0 Contributors, 2020. SciPy 1.0: Fundamental Algorithms for Scientific Computing in Python. *Nat. Methods* 17:261–272.

37. Wes McKinney, 2010. Data Structures for Statistical Computing in Python. *In* Stéfan van der Walt, and Jarrod Millman, editors, Proceedings of the 9th Python in Science Conference. 56 – 61.

38. Hunter, J. D., 2007. Matplotlib: A 2D graphics environment. *Comput. Sci. Eng.* 9:90–95.

39. Waskom, M. L., 2021. seaborn: statistical data visualization. *J. Open Source Softw.* 6:3021.

40. Pedregosa, F., G. Varoquaux, A. Gramfort, V. Michel, B. Thirion, O. Grisel, M. Blondel, P. Prettenhofer, R. Weiss, V. Dubourg, J. Vanderplas, A. Passos, D. Cournapeau, M. Brucher, M. Perrot, and D. Édouardand, 2011. Scikit-learn: Machine Learning in Python. *J. Mach. Learn. Res.* 12:2825–2830.

41. Yao, M., A. Tijore, D. Cheng, J. V. Li, A. Harihan, B. Martinac, G. T. V. Nhieu, C. D. Cox, and M. Sheetz, 2022. Force-dependent recruitment of Piezo1 drives focal adhesion maturation and calcium entry in normal but not tumor cells. *bioRxiv* .

42. Gudipaty, S. A., J. Lindblom, P. D. Loftus, M. J. Redd, K. Edes, C. F. Davey, V. Krishnegowda, and J. Rosenblatt, 2018. A Feedforward Mechanism Mediated by Mechanosensitive Ion Channel PIEZO1 and Tissue Mechanics Promotes Glioma Aggression. *Neuron* 100:799–815.e7.

43. Nicolson, G. L., 2014. The Fluid—Mosaic Model of Membrane Structure: Still relevant to understanding the structure, function and dynamics of biological membranes after more than 40years. *Biochim. Biophys. Acta* 1838:1451–1466.

44. Bohórquez-Hernández, A., E. Gratton, J. Pacheco, A. Asanov, and L. Vaca, 2017. Cholesterol modulates the cellular localization of Orai1 channels and its disposition among membrane domains. *Biochim. Biophys. Acta* 1862:1481–1490.

45. Abu-Arish, A., E. Pandzic, J. Goepp, E. Matthes, J. W. Hanrahan, and P. W. Wiseman, 2015. Cholesterol Modulates CFTR Confinement in the Plasma Membrane of Primary Epithelial Cells. *Biophys. J.* 109:85–94.

46. Romero, L. O., A. E. Massey, A. D. Mata-Daboin, F. J. Sierra-Valdez, S. C. Chauhan, J. F. Cordero-Morales, and V. Vásquez, 2019. Dietary fatty acids fine-tune Piezo1 mechanical response. *Nat. Commun.* 10:1200.

47. Bae, C., F. Sachs, and P. A. Gottlieb, 2011. The mechanosensitive ion channel Piezo1 is inhibited by the peptide GsMTx4. *Biochemistry* 50:6295–6300.

48. Höfling, F., and T. Franosch, 2013. Anomalous transport in the crowded world of biological cells. *Rep. Prog. Phys.* 76:046602.

49. Metzler, R., J.-H. Jeon, and A. Cherstvy, 2016. Non-Brownian diffusion in lipid membranes: Experiments and simulations. *Biochim. Biophys. Acta* 1858:2451–2467.

50. Vaisey, G., P. Banerjee, A. J. North, C. A. Haselwandter, and R. Mackinnon, 2022. Piezo1 as a force-through-membrane sensor in red blood cells. *bioRxiv* .

51. Kepten, E., I. Bronshtein, and Y. Garini, 2013. Improved estimation of anomalous diffusion exponents in single-particle tracking experiments. *Phys. Rev. E* 87:052713.

52. Martin, D. S., M. B. Forstner, and J. A. Käs, 2002. Apparent Subdiffusion Inherent to Single Particle Tracking. *Biophys. J.* 83:2109–2117.

53. Jacobson, K., E. D. Sheets, and R. Simson, 1995. Revisiting the Fluid Mosaic Model of Membranes. *Science* 268:1441–1442.

54. Saxton, M. J., and K. Jacobson, 1997. SINGLE-PARTICLE TRACKING:Applications to Membrane Dynamics. *Annu. Rev. Biophys. Biomol. Struct.* 26:373–399.

55. Shen, H., L. J. Tauzin, R. Baiyasi, W. Wang, N. Moringo, B. Shuang, and C. F. Landes, 2017. Single Particle Tracking: From Theory to Biophysical Applications. *Chem. Rev.* 117:7331–7376.

56. Simson, R., B. Yang, S. E. Moore, P. Doherty, F. S. Walsh, and K. A. Jacobson, 1998. Structural Mosaicism on the Submicron Scale in the Plasma Membrane. *Biophys. J.* 74:297–308.

57. Rajani, V., G. Carrero, D. E. Golan, G. de Vries, and C. W. Cairo, 2011. Analysis of Molecular Diffusion by First-Passage Time Variance Identifies the Size of Confinement Zones. *Biophys. J.* 100:1463–1472.

58. Monnier, N., S.-M. Guo, M. Mori, J. He, P. Lénárt, and M. Bathe, 2012. Bayesian Approach to MSD-Based Analysis of Particle Motion in Live Cells. *Biophys. J.* 103:616–626.

59. He, W., H. Song, Y. Su, L. Geng, B. J. Ackerson, H. B. Peng, and P. Tong, 2016. Dynamic heterogeneity and non-Gaussian statistics for acetylcholine receptors on live cell membrane. *Nat. Comm.* 7.

60. Golan, Y., and E. Sherman, 2017. Resolving mixed mechanisms of protein subdiffusion at the T cell plasma membrane. *Nat. Commun.* 8:1–15.

61. Kowalek, P., H. Loch-Olszewska, and J. S. Szwabi´nski, 2019. Classification of diffusion modes in single-particle tracking data: Feature-based versus deep-learning approach. *Phys. Rev. E* 100:32410.

62. Weron, A., J. Janczura, E. Boryczka, T. Sungkaworn, and D. Calebiro, 2019. Statistical testing approach for fractional anomalous diffusion classification. *Phys. Rev. E* 99.

63. Granik, N., L. E. Weiss, E. Nehme, M. Levin, M. Chein, E. Perlson, Y. Roichman, and Y. Shechtman, 2019. Single-Particle Diffusion Characterization by Deep Learning. *Biophys. J.* 117:185–192.

64. Janczura, J., P. Kowalek, H. Loch-Olszewska, J. Szwabiński, and A. Weron, 2020. Classification of particle trajectories in living cells: Machine learning versus statistical testing hypothesis for fractional anomalous diffusion. *Phys. Rev. E* 102:032402.

65. Muñoz-Gil, G., M. A. Garcia-March, C. Manzo, J. D. Martín-Guerrero, and M. Lewenstein, 2020. Single trajectory characterization via machine learning. *New J. Phys.* 22:013010.

66. Pinholt, H. D., S. S. Bohr, J. F. Iversen, W. Boomsma, and N. S. Hatzakis, 2021. Single-particle diffusional fingerprinting: A machine-learning framework for quantitative analysis of heterogeneous diffusion. *Proc. Natl. Acad. Sci. U.S.A.* 118:e2104624118.

67. Bailey, D. M., M. A. Catron, O. Kovtun, R. L. Macdonald, Q. Zhang, and S. J. Rosenthal, 2018. Single Quantum Dot Tracking Reveals Serotonin Transporter Diffusion Dynamics are Correlated with Cholesterol-Sensitive Threonine 276 Phosphorylation Status in Primary Midbrain Neurons. *ACS Chem. Neurosci* 9:2534–2541.

68. Adkins, E. M., D. J. Samuvel, J. U. Fog, J. Eriksen, L. D. Jayanthi, C. B. Vaegter, S. Ramamoorthy, and U. Gether, 2007. Membrane Mobility and Microdomain Association of the Dopamine Transporter Studied with Fluorescence Correlation Spectroscopy and Fluorescence Recovery after Photobleaching. *ACS Biochemistry* 46:10484–10497.

69. Gnanasambandam, R., C. Ghatak, A. Yasmann, K. Nishizawa, F. Sachs, A. S. Ladokhin, S. I. Sukharev, and T. M. Suchyna, 2017. GsMTx4: Mechanism of Inhibiting Mechanosensitive Ion Channels. *Biophys. J.* 112:31–45.

70. Syeda, R., J. Xu, A. E. Dubin, B. Coste, J. Mathur, T. Huynh, J. Matzen, J. Lao, D. C. Tully, I. H. Engels, H. Michael Petrassi, A. M. Schumacher, M. Montal, M. Bandell, and A. Patapoutian, 2015. Chemical activation of the mechanotransduction channel Piezo1. *eLife* 4:e07369.

71. Wijerathne, T. D., A. D. Ozkan, and J. J. Lacroix, 2022. Yoda1's energetic footprint on Piezo1 channels and its modulation by voltage and temperature. *Proc. Natl. Acad. Sci. U.S.A.* 119:e2202269119.

72. Botello-Smith, W. M., W. Jiang, H. Zhang, A. D. Ozkan, Y.-C. Lin, C. N. Pham, J. J. Lacroix, and Y. Luo, 2019. A mechanism for the activation of the mechanosensitive Piezo1 channel by the small molecule Yoda1. *Nat. Commun.* 10:4503.

73. Mosqueira, A., P. A. Camino, and F. J. Barrantes, 2018. Cholesterol modulates acetylcholine receptor diffusion by tuning confinement sojourns and nanocluster stability. *Sci. Rep.* 8.

74. Trimble, W. S., and S. Grinstein, 2015. Barriers to the free diffusion of proteins and lipids in the plasma membrane. *J. Cell Biol.* 208:259–271.

75. Saxton, M. J., 1993. Lateral diffusion in an archipelago. Single-particle diffusion. *Biophys. J.* 64:1766–1780.

76. Katz, M. J., and E. B. George, 1985. Fractals and the analysis of growth paths. *Bull. Math. Biol.* 47:273–286.

SUPPLEMENTARY MATERIAL

Mapping SPT trajectories to geometric features

In the context of SPT, the trajectory of a tagged particle is represented by an ordered sequence of N two-dimentional position vectors sampled at a constant time interval, Δt,

$$\vec{x}(t) = \{\vec{x}_1, \vec{x}_2 \ldots, \vec{x}_N\} \tag{1}$$

where $\vec{x}_i = (x_i, y_i) \in \mathbb{R}^2$ is the position vector at time $t = i\Delta t$, $i = 1 \ldots N$.

A trajectory *step* is the difference between consecutive position vectors $\vec{s}_i = \vec{x}_{i+1} - \vec{x}_i$. Therefore, a trajectory can also be described by the sequence of the $N - 1$ corresponding steps,

$$\vec{x}(t) \equiv \{\vec{s}_1, \vec{s}_2 \ldots, \vec{s}_{N-1}\} \tag{2}$$

We mapped each SPT trajectory to a six-dimensional *feature* vector: $(\Delta x, S, R_g, a, k, D_f)$, whose components (net displacement, straightness, radius of gyration, asymmetry, kurtosis, and fractal dimension) describe different geometric aspects of the trajectory.(33, 34)

Net Displacement

Net displacement, Δx, is the Euclidean distance of the trajectory final position to the initial position,

$$\Delta x = \sqrt{(x_N - x_1)^2 + (y_N - y_1)^2} \tag{3}$$

Straightness

Straightness, S, is a measure of the average direction change between consecutive steps, defined as (33)

$$S = \frac{1}{N-2} \sum_{i=1}^{N-2} \frac{\vec{s}_i \cdot \vec{s}_{i+1}}{|\vec{s}_i||\vec{s}_{i+1}|} \tag{4}$$

Radius of Gyration and Asymmetry

The trajectory's gyration tensor is the covariance matrix (75),

$$\mathrm{T} = \begin{pmatrix} \langle x^2 \rangle - \langle x \rangle^2 & \langle xy \rangle - \langle x \rangle \langle y \rangle \\ \langle xy \rangle - \langle x \rangle \langle y \rangle & \langle y^2 \rangle - \langle y \rangle^2 \end{pmatrix} \tag{5}$$

where $\langle \ldots \rangle$ denotes the mean of its argument (e.g. $\langle x \rangle = \sum_{i=1}^{N} x_i$). The gyration tensor is a symmetric 2-by-2 matrix,

$$\begin{pmatrix} T_{xx} & T_{xy} \\ T_{xy} & T_{yy} \end{pmatrix}$$

with eigenvalues

$$\lambda_{1,2} = \frac{(T_{xx} + T_{yy}) \pm \sqrt{(T_{xx} - T_{yy})^2 - 4T_{xy}^2}}{2} \tag{6}$$

The radius of gyration, R_g, is a measure of the overall extent of the trajectory, defined by

$$R_g^2 = \lambda_1 + \lambda_2 \tag{7}$$

Substituting (6) in (7) leads to

$$R_g^2 = (\langle x^2 \rangle - \langle x \rangle^2) + (\langle y^2 \rangle - \langle y \rangle^2) \tag{8}$$

which is equivalent to equation (1) in the main text.

The asymmetry, a, measures the elongation of the trajectory. We use the definition proposed by Helmuth et al. (33)

$$a = -\log\left(1 - \frac{(\lambda_1 - \lambda_2)^2}{2(\lambda_1 + \lambda_2)^2}\right) \tag{9}$$

Kurtosis

Kurtosis, k, is the standardized central fourth moment of a probability distribution. It measures whether a distribution is heavy-tailed in reference to a normal distribution. Here, we use it as a descriptor for the distribution of trajectory steps projected onto the gyration tensor's major principal axis. The major principal axis is the direction of the eigenvector $\vec{v}$ corresponding to the largest eigenvalue. In this case, $\mathrm{T}\vec{v} = \lambda_1 \vec{v}$. The kurtosis feature is then given by:

$$k = (N-1)\frac{\sum_{i=1}^{N-1}(s_i - \langle s_i \rangle)^4}{\left(\sum_{i=1}^{N-1}(s_i - \langle s_i \rangle)^2\right)^2} \tag{10}$$

where $s_i = \vec{s}_i \cdot \vec{v}$ and $\langle s_i \rangle = \frac{1}{N-1}\sum_{i=1}^{N-1} s_i$.

Fractal Dimension

The trajectory's fractal dimension is defined as (76)

$$D_f = \frac{\log(N-1)}{\log(N-1) + \log(\frac{d}{L})} \tag{11}$$

where d denotes the largest distance between any two trajectory positions, and $L = \sum_{i=1}^{N} s_i$ denotes the total length of the trajectory. It is a measure of the degree to which the trajectory is space-filling. A straight line has $D_f = 1$; any other planar curve will have $D_f > 1$. A two-dimensional random walk has $D_f = 2$. A trajectory constrained to a limited area may have multiple overlaps and therefore will have $D_f > 2$.

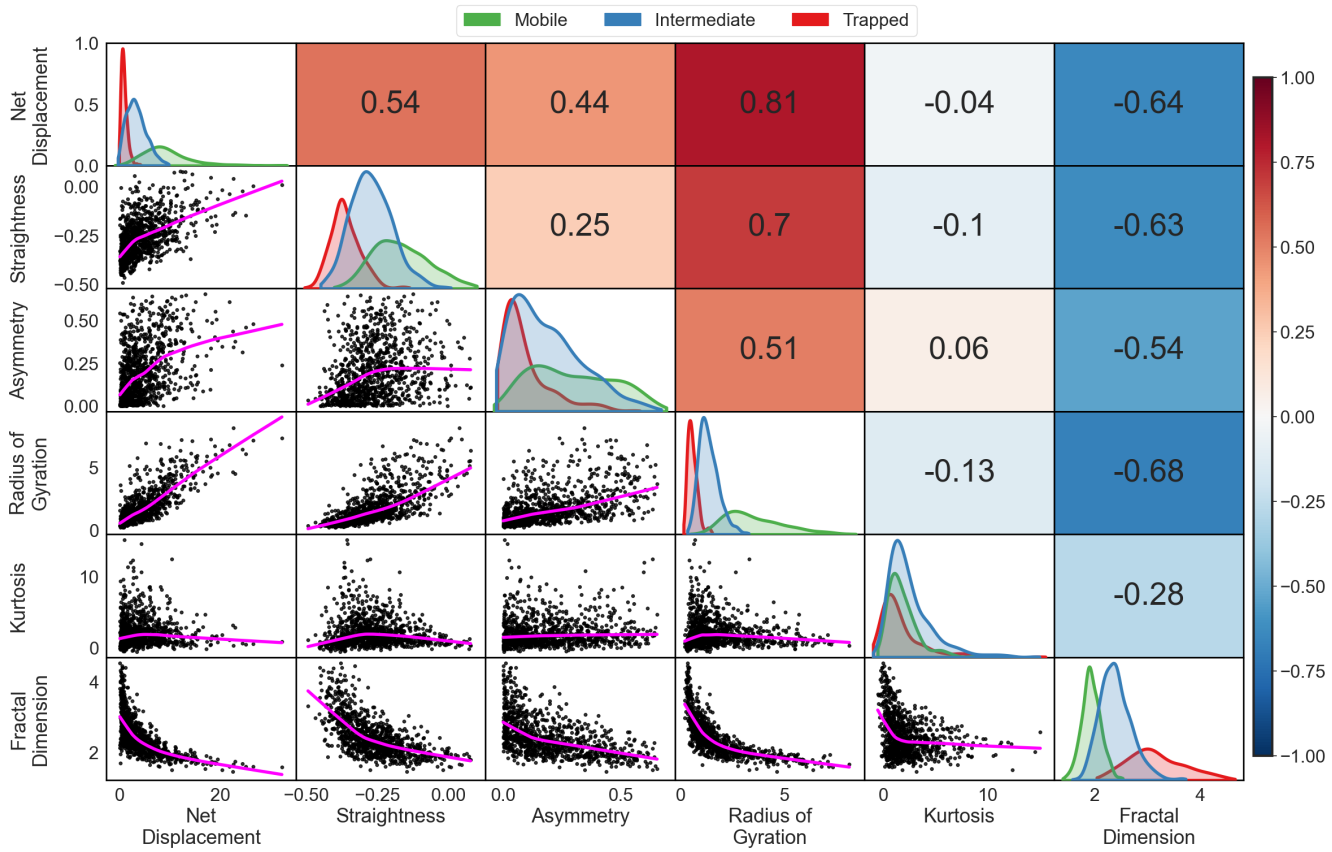

Supplementary Figure 1: Correlation matrix plot of geometric features used for automated trajectory classification calculated from a 1000-trajectory data set classified by visual inspection. The diagonal elements show kernel density estimates of of each feature distribution separated by their labeled class (“mobile,” green; “intermediate,” blue; “trapped,” red). The relationships between pairs of features are shown as scatter plots below the diagonal. A locally weighted scatterplot smoothing trend line is shown in magenta. The corresponding Pearson correlation coefficients are shown above the diagonal colored according to a BWR color scale.

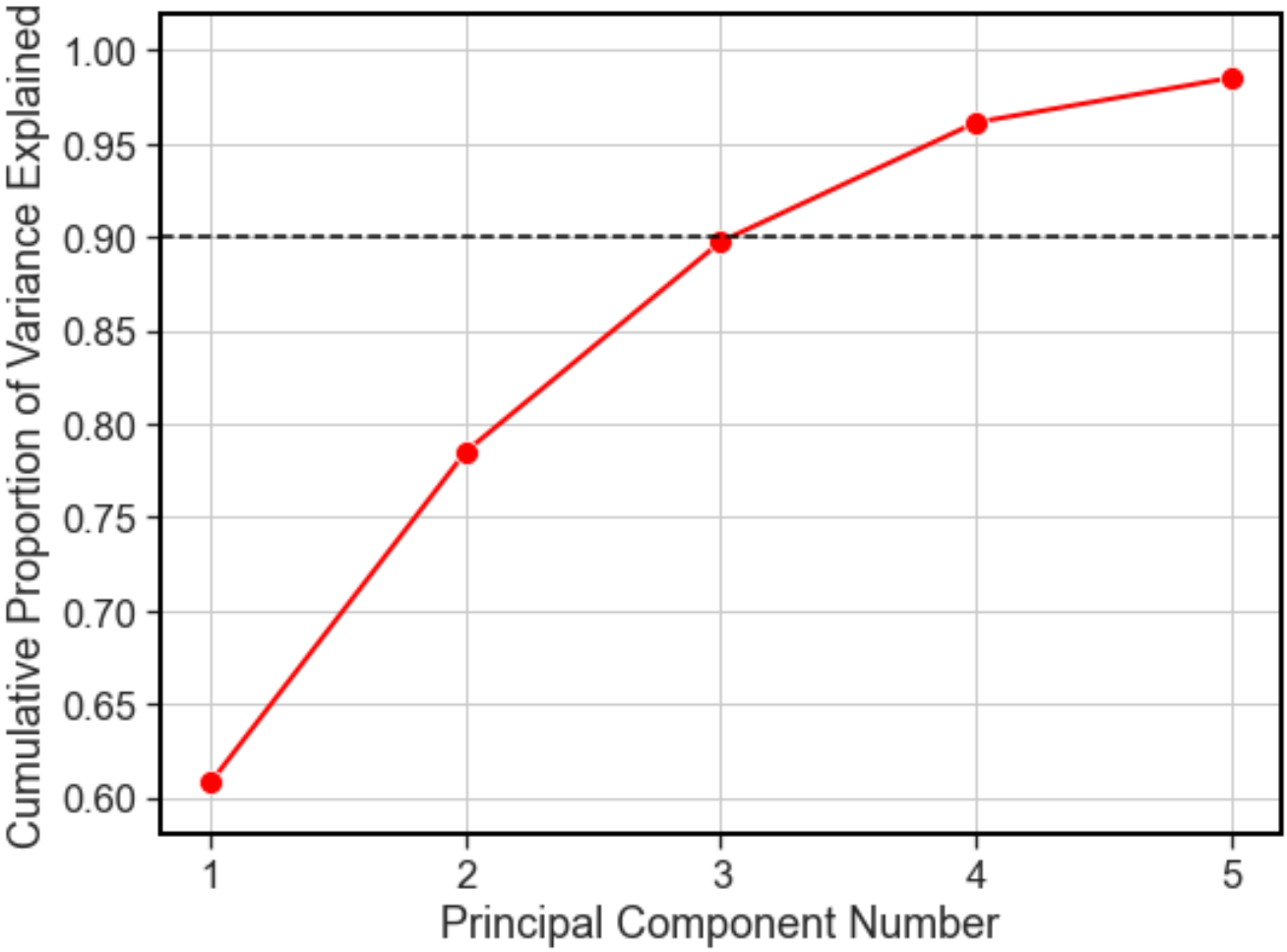

Supplementary Figure 2: Cummulative proportion of variance explained by the principal components of the six-dimensional geometric feature vectors generated from the 1000-trajectory data set classified by visual inspection. The horizontal dashed line indicates that 90% of the variance six-dimensional data set is explained by the first three principal components.

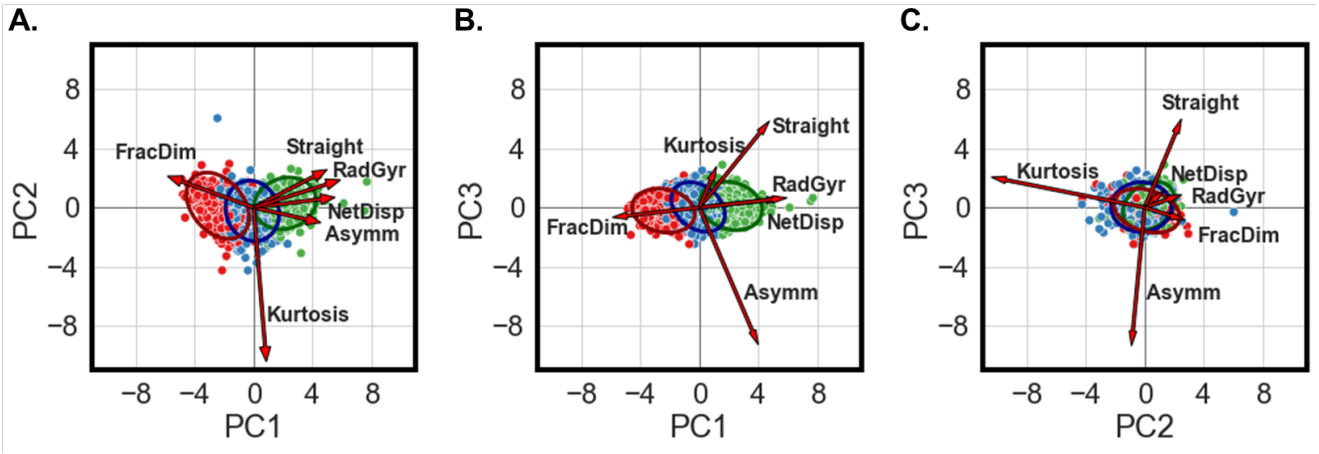

Supplementary Figure 3: Principal component analysis biplots of the six-dimensional geometric feature vectors generated from the 1000-trajectory data set classified by visual inspection. The projections of the 1000 observations onto each subspace are shown as dots colored by class (“mobile,” green; “intermediate,” blue; “trapped”, red). The three classes are largely separated along the first principal component (PC1) into three overlapping groups, as evidenced by the 95% confidence ellipses for each class with limited contributions from PC2 and PC3. The red arrows show the projection of the original features onto each subspace (scaled up by a factor of 10). The largest contributions to PC1 are from net displacement, radius of gyration, and fractal dimension, all of which characterize the trajectory spread. Limited separation between classes in the PC2-PC3 plane (panel C) indicates that including additional principal components would not improve trajectory segregation, justifying the choice of a three-dimensional principal components subspace for training. Panel A is also shown in Figure 2A

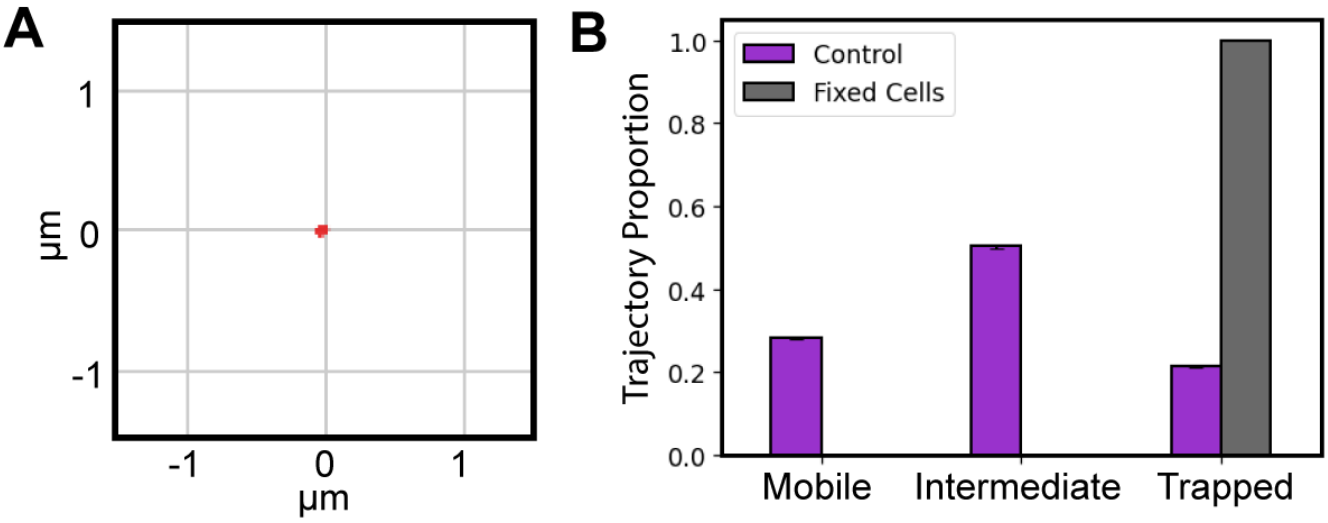

Supplementary Figure 4: Piezo1-tdTomato in fixed MEFs are classified as “trapped” by the SVM. A. Representative Piezo1-tdTomato trajectory (red) from a fixed Piezo1-tdTomato MEF showing a highly limited spatial extent. B. Almost all the trajectories from a fixed Piezo1-tdTomato MEF data set are identified as “trapped” by the SVM. Also shown in Fig.2C

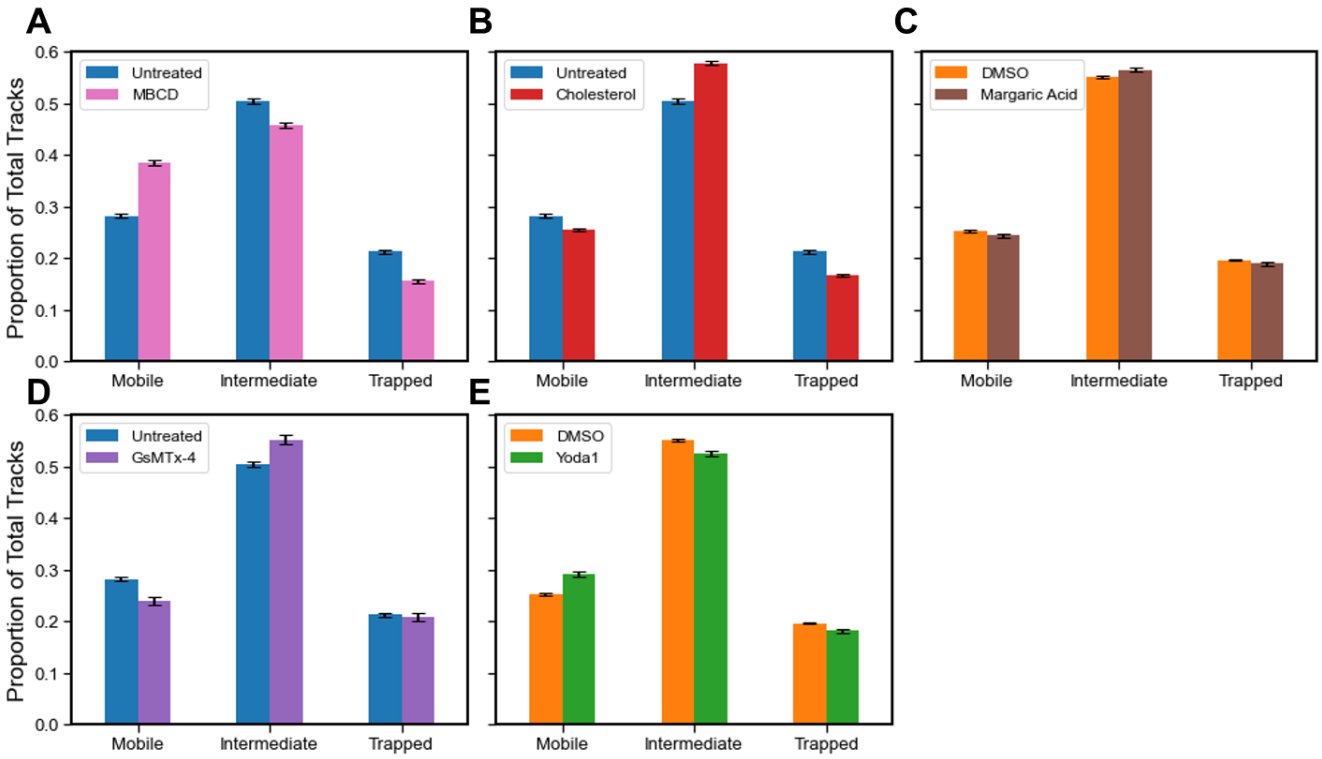

Supplementary Figure 5: Trajectory proportions resulting from the SVM classification of Piezo1-tdTomato trajectories under various conditions. A. MBCD treatment (pink) results in an increase in the "mobile" proportion of trajectories relative to the untreated control (blue). B. Cholesterol-MBCD treatment (red) results in a decrease in the "mobile" proportion of trajectories relative to the untreated control (blue). C. Margaric acid treatment (brown) results in a decrease in the "mobile" proportion of trajectories relative to the DMSO control (orange). D. GsMTx-4 treatment (purple) results in a decrease in the "mobile" proportion of trajectories relative to the untreated control (blue). E. Yoda1 treatment (green) results in an increase in the "mobile" trajectories relative to the DMSO-treated control (orange). The SVM was trained as three separate binary classifiers. Thus, we interpret the bar heights within one plot as the sample proportions for each class. The error bars are the corresponding standard errors.

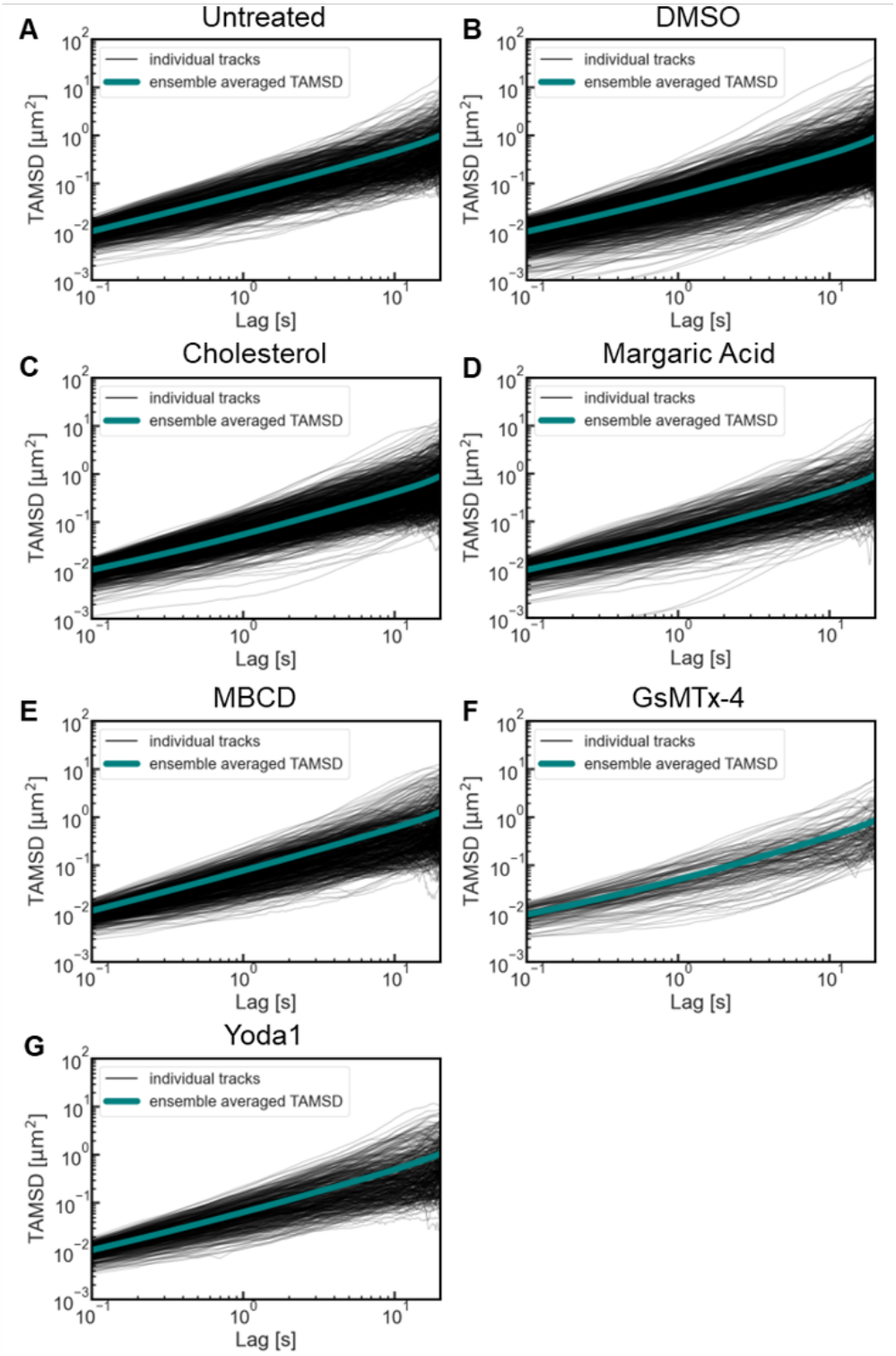

Supplementary Figure 6: TAMSD as a function of lag time of Piezo1-tdTomato expressed in MEFs (individual "mobile" trajectories, black; ensemble average, green). A. Untreated MEFs (also shown in Fig.4A). B. DMSO-treated. C. 100 µg/mL cholesterol-MBCD-treated. D. 150 µM margaric acid-treated E. 10 mM MBCD-treated. F. 4 µM GsMTx-4-treated and G. 4 µM Yoda1-treated.

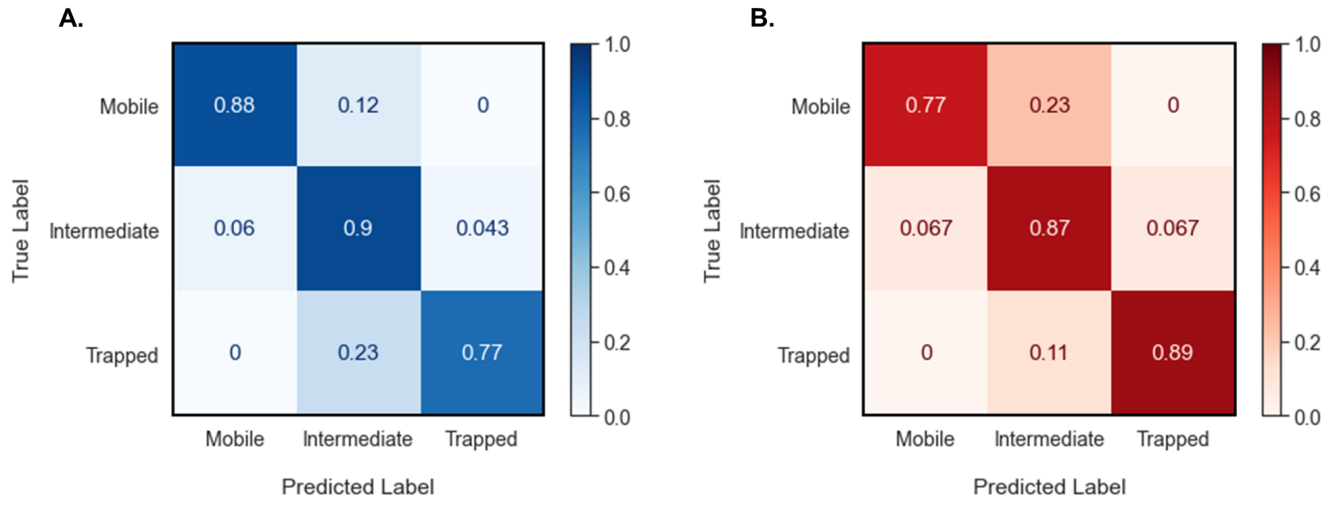

Supplementary Figure 7: SVM performance evaluation via confusion matrices. Confusion matrices for testing (A), and training data (B) show adequate separation between classes with an average F1-score of 0.87.